

Decelerated non-relativistic expansion in a tidal disruption event with a potential neutrino association

Prashanth Mohan^{1,*}, Tao An^{1,*}, Yingkang Zhang¹, Jun Yang², Xiaolong Yang¹, Ailing Wang^{1,3}

¹*Shanghai Astronomical Observatory, Key Laboratory of Radio Astronomy, Chinese Academy of Sciences, Nandan Road 80, 200030, China*

²*Department of Space, Earth and Environment, Chalmers University of Technology, Onsala Space Observatory, SE-439 92 Onsala, Sweden*

³*University of Chinese Academy of Sciences, 19A Yuquanlu, Beijing 100049, China*

A tidal disruption event (TDE) involves the tidal shredding of a star in the vicinity of a dormant supermassive black hole. The nearby (≈ 230 mega-parsec) radio-quiet (radio luminosity of $4 \times 10^{38} \text{ erg s}^{-1}$) AT2019dsg is the first TDE potentially associated with a neutrino event. The origin of the non-thermal emission in AT2019dsg remains inconclusive; possibilities include a relativistic jet or a sub-relativistic outflow. Distinguishing between them can address neutrino production mechanisms. High resolution very long baseline interferometry monitoring provides uniquely constraining flux densities and proper motion of the ejecta. A non-relativistic (outflow velocity of $\approx 0.1 c$) decelerated expansion in a relatively dense environment is found to produce the radio emission. Neutrino production may be related to the acceleration of protons by the outflow. The present study thus helps exclude jet-related origins for the non-thermal emission and neutrino production, and constrains non-jetted scenarios.

*Corresponding author

When a star passes within the tidal radius of a formerly dormant supermassive black hole (SMBH of mass $M_{\bullet} = 10^6 - 10^8 M_{\odot}$, where M_{\odot} is the solar mass), its destruction by tidal forces leads to the fallback accretion of stellar debris^{1,2}. This usually powers a thermal flare in optical, ultra-violet (UV) and X-ray bands, with a luminosity comparable to bright Supernovae at $\approx 10^{43} - 10^{44} \text{ erg s}^{-1}$ (³). The bolometric luminosity generally declines with a power law index of $-5/3$ (³) over months to years, indicative of fallback accretion^{2,4}. However, individual bands can deviate from this trend. The later phase (months to years) decline in the X-ray and UV bands may be more shallow (with an index of $-5/12$) and is indicative the prevalence of disk emission⁵. The most gravitationally bound stellar debris can shock the loosely bound material accreted onto the SMBH on its return near the pericentre over a fallback timescale of ten to hundred days, thus launching a spherical mildly relativistic outflow^{6,7}. Upon interaction with the surrounding circum-nuclear medium (CNM), the outflow produces a non-thermal, pre-dominantly synchrotron afterglow emission^{8,9}. Multi-wavelength observations of the afterglow can help identifying the onset of this interaction and constrain the energy output from the TDE and the properties of the CNM¹⁰.

The transient AT2019dsg was discovered on 2019 April 9 by the Zwicky Transient Factory¹¹ and identified as a TDE in a host galaxy at a redshift of $z = 0.051$ ^{12,13}, making it a rarely-seen nearby TDE. A recent study¹⁴ reported on a putative association of AT2019dsg with the 0.2 peta electron volt (PeV) energy neutrino event IC191001A, which was detected by the IceCube neutrino observatory on 2019 October 1 (175 days after the TDE discovery¹⁵) and is expected to be of astrophysical origin. A multi-wavelength analysis in the same study¹⁴ indicates a highly luminous

TDE (optical peak luminosity of $\approx 3.5 \times 10^{44} \text{ erg s}^{-1}$) and suggests the presence of an active central engine embedded in an optically thick photosphere, which powers sub-relativistic outflows and provides a suitable site for the production of neutrinos. Optical polarimetric observations¹⁶ show a decrease in linear polarisation degree from 9.6 per cent near the optical peak around 2019 May 17 to 2.7 per cent on 2019 June 20 during the declining phase; this variation is ascribed to a non-isotropic accretion disk or a relativistic jet. The concordance scenario¹⁷ proposes the presence of a relativistic jet that participates in the acceleration of protons and provides the necessary site for the production of neutrinos. Alternatively, an off-axis jet may host hadronic interactions and the neutrino production site¹⁸. An analysis of multi-wavelength radio observations of AT2019dsg¹⁹ suggests that the emission originates from the interaction of a non-relativistic outflow with the surrounding medium. Based on the relatively low outflow velocity and energy output in the context of TDEs and Type Ib/c Supernovae, the study in Ref. [19] suggests that the neutrino association is less likely. The complex observational signatures and associated deductions are thus inconclusive on the origin of the non-thermal emission, which may originate either from a relativistic jet or a non-relativistic outflow. Clearly distinguishing between them is crucial in constraining the TDE properties (physical and geometric properties of the SMBH and disrupted stellar system), the nuclear environment of the host galaxy, the central engine activity and in clarifying the neutrino production mechanisms.

Very long baseline interferometry (VLBI) observations at milli-arcsecond (mas) resolutions can help measure the size of the radio afterglow, constrain the proper motion of the emitting component^{9,20}, and provide inputs for discerning the TDE and CNM properties. Radio emission has

been detected in a total of nine TDEs¹⁰. Of these, only a few have been imaged using VLBI, with large differences in radio luminosity evolution, environmental properties, and the level of collimation of the outflow. Besides, extensive monitoring campaigns have only been conducted on *Swift* J1644+5734^{9,21–26} and Arp 299-B AT1⁷ owing to the presence of a relativistic jet, and ASASSN-14li^{27–30} being relatively close proximity ($z = 0.02$). A multi-wavelength observation campaign was carried out to study AT2019dsg and its host galaxy³¹. The results include the inference of a central SMBH of $5.4 \times 10^6 M_{\odot}$, derived from the optical spectroscopy. They additionally report the detection of a compact source with no significant displacement (one sigma astrometric uncertainty of ≈ 6 mas) from the phase centre, as inferred from the 5 and 1.4-GHz radio monitoring observations made by the electronic Multi-Element Remotely Linked Interferometer Network (*e*-MERLIN) up to 180 days after the TDE.

We employ the VLBI technique to monitor any emission structure change of AT2019dsg at high resolutions, motivated by potentially identifying a (collimated) relativistic jet and determining the source size. This makes it one of only three thermal emission dominated TDEs with VLBI monitoring, the others being ASASSN-14li²⁸ and CNSS J0019+00³². Our observations were carried out with the European VLBI Network (EVN) at 5 GHz spanning three epochs at 200, 216 and 304 days after the TDE, respectively and covered the declining phase of the source radiative evolution. As the source was successfully detected in all three epochs, this provides unique constraining information: flux densities with little contamination from the host galaxy, and kinematics including source size, and astrometry to infer any significant proper motion. Details of the observation logs are presented in Table 1. The first and third observations were made in the standard

disk-recording mode, involving a maximum of 20 telescopes. The second observation was made in the electronic-VLBI mode (*e*-EVN). The effective offset of the emission peak away from the phase centre remains unchanged at the $3\text{-}\sigma$ level (< 0.6 mas), indicating the absence of a statistically significant proper motion in AT2019dsg. Based on the smallest measurable offset in the source position of 0.14 mas over a time span of 304 days (upto the third epoch), any significant proper motion larger than 0.16 mas yr^{-1} (or $0.57 c^1$) can be ruled out. The EVN images of AT2019dsg during the three epochs and the constraints on the peak emission positions with respect to the phase centre are presented in Figure 1. With an afterglow size R evolving with observation time t as $R \propto t^\alpha$, the velocity $v \propto t^{\alpha-1}$. Using $v \leq 0.57 c$, $\alpha \leq 0.65$; thus, the sub-relativistic expansion is currently decelerating, likely owing to the central engine shutting off at later epochs. The non-detection of an apparent superluminal jet (albeit, during the later epochs) makes it imperative to understand the origin of radio emission. High brightness temperatures of $\sim 10^9$ K and $\geq 10^8$ K during the first and third epochs, and the detection of an unresolved compact structure indicate the presence of a non-thermal component. This is consistent with afterglow emission from the interaction of an outflow with the surrounding CNM, which produces an expanding forward shock.

The compiled 5-GHz light curve consists of flux densities reported in literature, and the measurements from our EVN observations. A smoothly broken power law is used to fit the light curve (see Methods), presented in Figure 2. A peak flux density F_{ν_p} of 1.2 ± 0.1 mJy at a time

¹Assuming a flat cosmology with parameters $H_0 = 70 \text{ km s}^{-1} \text{ Mpc}^{-1}$, $\Omega_m = 0.27$, $\Omega_\Lambda = 0.73$, at $z = 0.051$, an angular separation of 1 mas corresponds to a projected size of $\approx 1 \text{ pc}$ ³³, and a proper motion of 1 mas yr^{-1} corresponds to an expansion speed of $3.4 c$.

t_p of $159.9_{-6.9}^{+7.8}$ days is inferred. The power law indices during the rising and declining phases are $\alpha_1 = 2.1_{-0.5}^{+0.6}$ and $\alpha_2 = -2.0_{-0.4}^{+0.3}$ respectively. For an expanding forward shock with a constant electron injection energy index p , the time dependence of size $R \propto t^\alpha$, of magnetic field strength $B \propto R^{-2} \propto t^{-2\alpha}$ and the proportionality constant (for the number of electrons per unit energy within the region) $N_0 \propto B^2 \propto t^{-4\alpha}$ result in optically thick and thin flux densities that scale as $\propto t^{3\alpha}$ and $\propto t^{-(2+p)\alpha}$ respectively. With the lower limit of $\alpha_1 = 1.6$, $\alpha \geq 0.53$. Using $\alpha \approx 0.5$ and the declining phase index of -2.0 yields a $p \approx 2$. The corresponding optically thin spectral index then depends on the observation frequency as $\propto \nu^{-(p-1)/2} \propto \nu^{-0.5}$, a relatively flat spectrum; the expansion thus may have been supported in the past through injection from the central engine as previously reported ¹⁴. The radio luminosity at 5 GHz is then $\nu L_\nu \approx 4\pi D_L^2 F_{\nu_p} (1+z)^{-(1-\alpha)} \approx 3.6 \times 10^{38} \text{ erg s}^{-1}$. This makes AT2019dsg relatively radio-quiet¹⁰ and comparable to ASASSN-14li ^{10,28} and CNSS J0019+00³², whose radio emission is likely to be associated with a non-relativistic outflow. We then use a $p = 2.01$ in subsequent calculations. The VLBI measured flux densities and constraint on proper motion thus play a complementary role in enabling inferences on the emission source nature, and helping reduce the number of free parameters in the synchrotron radiation model.

The total energy in the outflow is minimal when the energy densities of the relativistic electrons accelerated by the forward shock and that of the magnetic field are in equipartition ^{34,35}. The peak flux density is assumed to correspond to the transition of the synchrotron self-absorption frequency ν_a through the observation band. The evaluated peak flux density and associated time are then used to estimate the minimal size, magnetic field strength, energy output and ambient medium

number density; all of these parameters are appropriate for a non-relativistic expansion ^{32,35} (see Methods). The application involves a sensitive dependence on microphysical parameters including the fraction of the total energy density in the electron kinetic energy ϵ_e and magnetic field ϵ_B . We use (ϵ_e, ϵ_B) of $(1/3, 1/3)$ and $(0.1, 0.01)$ as typically representative of TDEs and AT2019dsg, respectively ^{19,32,36}.

The frequencies that mark transitions in the evolving spectrum and their time evolution are: the self-absorption frequency $\nu_a \propto t^{-2\alpha(p+5)/(p+4)}$ (e.g., $\nu_a \propto t^{-7\alpha/3}$ for $p = 2$), the synchrotron frequency $\nu_m \propto t^{-2\alpha}$, and the synchrotron cooling frequency $\nu_c \propto t^{6\alpha-2}$. With these dependencies and using the above microphysical parameters, the frequencies at $t = t_p$ are $\nu_a = 4.83 \times 10^9$ Hz, $\nu_m = (0.2 - 4.1) \times 10^7$ Hz and $\nu_c = (1.2 - 5.9) \times 10^{11}$ Hz. The estimated ν_a at t_p (which coincides with the observation band) and the ordering $\nu_m \ll \nu_a$ are consistent with the expectation for a non-relativistic outflow. The minimal values of the equipartition size is $R_{eq} = (5.1 - 5.9) \times 10^{16}$ cm ($3.2 - 3.7 \times 10^4 R_S$ where $R_S = 1.59 \times 10^{12}$ cm is the Schwarzschild radius of a $5.4 \times 10^6 M_\odot$ SMBH), magnetic field strength $B_{eq} = 0.24 - 0.42$ G, energy output $E_{eq} = (0.2 - 1.3) \times 10^{50}$ erg, and the ambient number density is $n_{eq} = (0.8 - 2.8) \times 10^2 \text{ cm}^{-3}$, indicating an energetic TDE (compared to thermal dominated TDEs)¹⁰ and an expansion into a relatively dense CNM. The total kinetic energy carried by a relativistic jet E_j can be related to the energy output by $E_j(\Gamma\theta_j)^2/2 = E_{eq}$ where Γ is the bulk Lorentz factor and θ_j is the jet half-opening angle. Assuming even a mildly relativistic jet with $\Gamma = 2$ and an $E_j = (3.2 - 5.9) \times 10^{52}$ erg (see Methods), $\theta_j = 0.8 - 2.6$ degrees. A higher Γ results in much more collimating θ_j implying that the presence of a relativistic jet is unlikely. As the outflow is inferred to accelerate in the early phase¹⁴, the outflow can have a

constant velocity in a short phase between the flux density peak ($t_p = 159.9$ d) and the first VLBI epoch (200 d), with a lower limit of $R_{eq}/t_p \approx 0.12 - 0.14 c$ for $t_p = 159.9$ d.

Using the equation for the outflow velocity, the mass of the disrupted star is found to be in the range $M_\star = 5.7 - 18.6 M_\odot$. For this estimate, we used a SMBH mass $M_\bullet = 5.4 \times 10^6 M_\odot$ and a penetration factor $\beta = 1$ (which characterizes the distance of the closest approach to the SMBH). The inferred mass outflow rate is $\approx 10^{-3} M_\odot \text{ yr}^{-1}$ (for $t = t_p$). A density contrast between the CNM and the outflow of ≥ 1.3 requires that the microphysical parameters $\epsilon_e = 0.1$ and $\epsilon_B \leq 0.01$ at $t = t_p$. This indicates a relatively denser CNM, consistent with the expectation from the equipartition analysis.

The outflow can originate either as a wind driven by radiation pressure from the accretion disk^{37,38} or as unbound debris from the stellar disruption³⁹. In the former scenario, the lifetime is ≈ 438 d and is set by the requirement that the shrinking photospheric radius equals the accretion disk size ($\approx 10 R_S$, R_S is the Schwarzschild radius of the black hole). The corresponding disk luminosity is ~ 0.2 times the Eddington luminosity which can support non-relativistic winds with velocities $\leq 0.2 c$ driven by radiation pressure from the disk emission³⁸. In the latter scenario, comparing the outflow velocity inferred here ($\approx 0.12 - 0.14 c$) and that associated with the outflow³⁹ yields a non-physical stellar mass of $\geq 2.5 \times 10^{14} M_\star$. An origin as radiatively driven winds is thus more likely.

The acceleration of ultra-high energy cosmic rays⁴⁰ are closely associated with mechanisms of neutrino production⁴¹. This is naturally enabled in the case of a relativistic jet, through hadronic

and photo-hadronic interactions^{41,42}. In the proposed concordance scenario¹⁷, the neutrino production is attributed to the interaction between X-ray photons (back-scattered from an expanding optically thick cocoon) and protons accelerated by internal shocks in a relativistic jet. As the density contrast is not especially large, a dark or hidden relativistic jet appears unlikely, also owing to the non-detection of a significant proper motion. For a relativistic jet with a bulk Lorentz factor equal to the Doppler boosting factor, the apparently superluminal velocity v_{\perp} is related to the jet viewing angle θ as $(v_{\perp}/c) = 1/\tan \theta$. For a $\theta = 10^{\circ} - 45^{\circ}$, $v_{\perp} = 1 - 5.67 c$ corresponding to a proper motion of $0.29 - 1.67 \text{ mas yr}^{-1}$ which exceeds our measurement of $\leq 0.16 \text{ mas yr}^{-1}$ thus rendering the proposed scenario for neutrino production by photo-hadronic interactions in a relativistic jet less likely.

We then explore non-jetted scenarios enabling the production of neutrinos. These include an association with the outflow or the accretion process^{43,44}, both of which are potential candidates but neither can achieve the expected all-neutrino fluence⁴⁴. A detailed exposition of the neutrino production is beyond the current scope. We thus discuss the relative plausibility of these scenarios broadly by estimating the maximum energy to which the protons (constituting the cosmic rays which produce the neutrinos through various reaction channels) can be accelerated and the associated timescales. In the former (outflow), the protons are accelerated by the outflow and the maximum energy⁴⁵ is $E_p \propto t^{-1} \leq 1.5 \times 10^{16} \text{ eV}$ (at a time $t = 175 \text{ d}$), limited by the dynamic timescale. The detected neutrino energy $E_{\nu} \approx 1.3 \%$ of E_p indicating that this is a likely channel. In the latter (accretion), the super-Eddington regime (with a lifetime $t_j \approx 568.1 - 1400 \text{ d}$) which follows the debris circularization ($\approx 9 \text{ d}$) is found to be inefficient in producing relativistic protons

as the cooling from proton-proton collisions effectively limits the maximum energy⁴³. In the radiatively inefficient accretion regime, the acceleration of protons by plasma turbulence is limited by their diffusion with a consequent maximum energy $E_p \leq 3.7 \times 10^{16}$ eV with the neutrino energy being $\approx 0.5\%$ of E_p . However, the timescale for transition from the super-Eddington to radiatively inefficient accretion flow is quite long ($\approx 16t_j \geq 9.1 \times 10^3$ d) rendering it unlikely to have set in during the current observation period. We thus tentatively favour the outflow scenario for the production of neutrinos.

The neutrino production itself may be enabled by either the $p\gamma$ or pp interactions at the base of the outflow, taken to be the photospheric radius $R_{ph} \approx 45.8 - 163.2 R_S$ (at $t = 175$ d). For an accretion disc of size $\approx 10 R_S$, R_{ph} is 4.6 — 16.3 times this size, indicating that the photosphere is outside and likely to be spatially distributed⁶ around the disc. This site provides a suitable cross section for the interactions with a particle number density $\geq 10^8 \text{ cm}^{-3}$ ⁽¹⁴⁾ for $\gamma \geq 2.1$ assuming that the CNM density scales as $R^{-\gamma}$ in the innermost region. Furthermore, at the same epoch, the number density of unbound stellar debris in the vicinity of the accretion disc is $\leq 4.24 \times 10^{11} \text{ cm}^{-3}$ thus providing support to this scenario. A production at the radio emission region at $R_{eq} \approx (5.1 - 5.9) \times 10^{16} \text{ cm}$ is unlikely owing to a relatively low particle number density $n_{eq} = (0.8 - 2.4) \times 10^2 \text{ cm}^{-3}$.

The VLBI observations cover the declining phase of the source evolution, and thus provide unique constraints on the flux densities and proper motion. These play a key role in inferring a decelerating non-relativistic expansion, and in reducing the free parameters in the radiative model.

The former result indicates an inactive central engine which may have been previously participating in energy injection to sustain the radio emission¹⁴. Similar to CNSS J0019+00 and ASASSN-14li, a relatively radio-quiet ($\approx 4 \times 10^{38} \text{ erg s}^{-1}$) nature of AT2019dsg with a predominantly thermal emission and the non-detection of a relativistic jet are consistent with that the non-thermal radio emission is from outflow activity. The relatively small density contrast (≥ 1.3), albeit during the later epochs hints at an outflow that may have naturally decelerated owing to the shutting off of the central engine rather than due to the frustration of the external CNM¹⁴.

Using the results together with the measured flux densities during the rising phase, the following scenario emerges: a star of $\approx 6 - 19 M_{\odot}$ is disrupted; a non-relativistic outflow with a velocity of $\approx 0.1 c$, originating from and radiatively driven by gas accretion onto the supermassive black hole interacts with the surrounding CNM at $\geq 5.1 \times 10^{16} \text{ cm}$ ($\geq 3.2 \times 10^4 R_S$); the interactions result in an expanding forward shock that accelerates ambient electrons (constituting the CNM) to relativistic energies, thus producing the observed synchrotron radio emission; the production of neutrinos is likely associated with the base of the outflow, where protons can be efficiently accelerated to Peta eV energies and provide suitable cross sections for hadronic or photo-hadronic interactions, consistent with such an expectation from a more detailed analysis¹⁴. This is in contrast to an origin from internal shocks in a relativistic jet¹⁷ or a non-expectation of neutrinos from AT2019dsg¹⁹.

As the VLBI observations offer high resolutions, they effectively help reduce contamination from the host galaxy and thus offer a complementary (to multi-wavelength electro-magnetic obser-

vations) but unique perspective on the source evolution. Studies of TDEs, especially those nearby, are crucial to probe the outflow nature and constrain the CNM properties of the galactic nuclear regions. This can help in understanding the dynamics of feeding stellar and gaseous material and clarify potential activity in the galactic nucleus. The inference of a non-relativistic outflow, and its potential role in the production of neutrinos provides an expanded inventory of extra-galactic sources of neutrinos. This includes blazar jets^{46,47}, the dominant non-blazar AGN populations^{48,49} and slow transients including gamma-ray bursts^{50,51}, making multi-messenger investigations of similar sources essential and exciting⁵². This could be relevant in planning strategies for multi-messenger studies with global facilities.

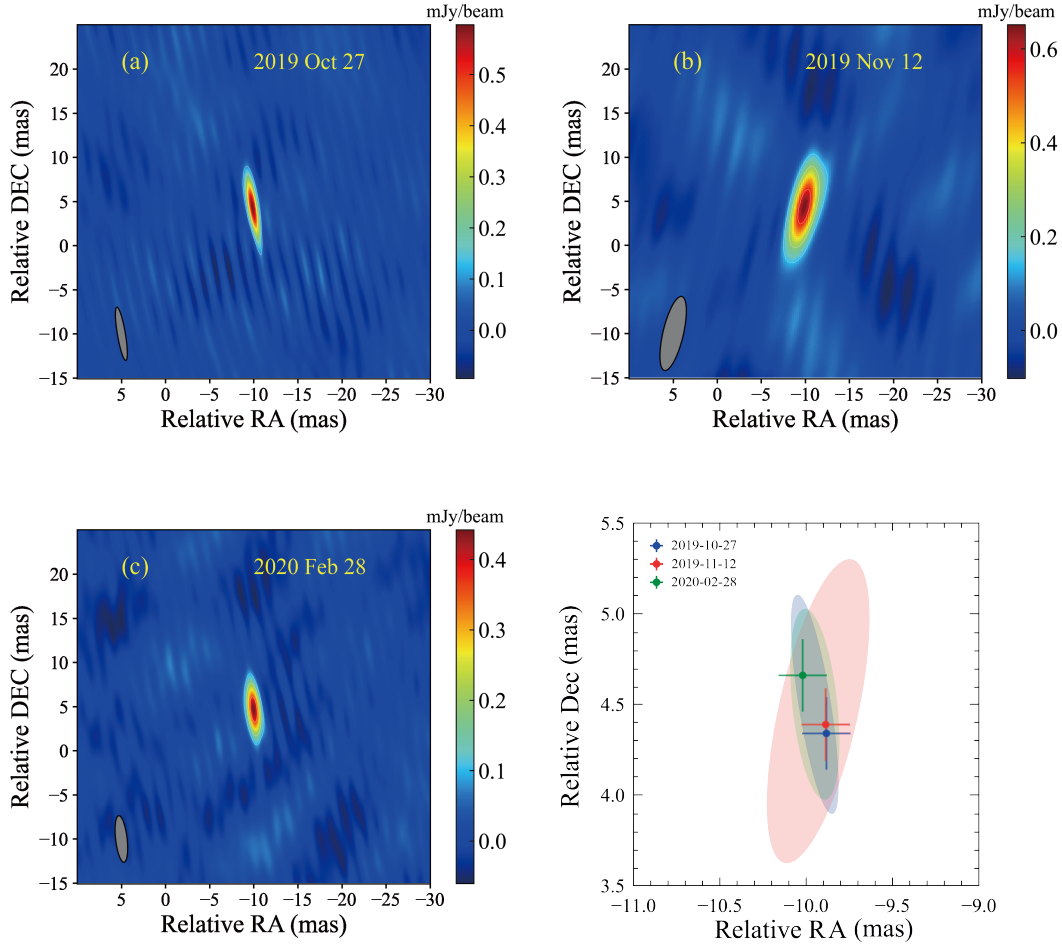


Figure 1: Top row and bottom left: high-resolution images from the three EVN observations showing a compact, unresolved emitting source. Bottom right: constraints on the source peak positions. The image centre is at right ascension (RA) $\alpha = 20^h 57^m 02^s.965$ and declination (Dec) $\delta = +14^\circ 12' 16''.290$ (J2000); the colour bar denotes the brightness scale. The imaging parameters are presented in Table 1. The peak positions are measured using the reference from the phase-referencing calibrator J2052+1619, with positional astrometric uncertainties of 0.14 mas and 0.20 mas along the RA and Dec directions, respectively. The variation of the peak position falls within one fifth of the restoring beam marked by the ellipse in the bottom-left corner of each panel.

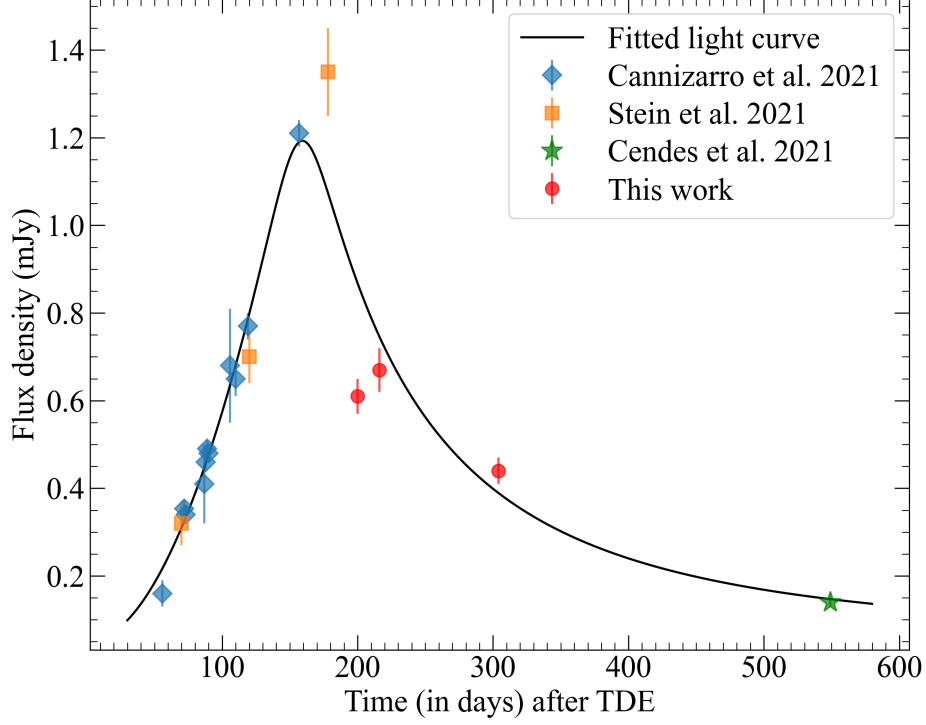


Figure 2: Compiled 5 GHz light curve fit with a smooth broken power-law plus a linear trend (see Methods). The blue and orange data points cover the rising phase and peak^{14,31} while the green data point¹⁹ helps constrain the declining phase slope. The red data points during the declining phase are from our EVN observations. The fit yields a rising slope α_1 of $2.10^{+0.59}_{-0.50}$, a declining slope α_2 of $-1.95^{+0.33}_{-0.36}$, peak flux density $F_{\nu_p} = 1.19 \pm 0.05$ mJy at a time $t_p = 159.89^{+7.76}_{-6.91}$ days.

Methods

VLBI observations and data reduction. The 5-GHz European VLBI network (EVN) observations were carried out on 2019 October 27 and November 12, and 2020 February 28. The observational setup is presented in Table 1. It includes the EVN project code, date, frequency, time duration, bandwidth and participating telescopes (which included a maximum of 20 VLBI telescopes). The longest baselines in the East-West (Yebes, Spain — Tianma, China) and North-South (Badary, Russia - Hartebeesthoek, South Africa) directions span up to ≈ 9000 km and 9800 km, respectively, contributing to the mas-scale high resolution. The large number of participating stations provided a good sampling in the (u, v) plane, optimally covering the source and a resulting high-sensitivity image with a root-mean-square (rms) noise down to ≈ 0.015 mJy beam $^{-1}$.

All the observations were conducted by utilising the phase-referencing technique⁵³. During the observations, J2052+1619 served as the primary phase-referencing calibrator (Cal1, ~ 200 mJy at 5 GHz), 2.37 degree away from the target source AT2019dsg (Tar) on the plane of the sky. The nearby 20-mJy source J2058+1512 was used as the secondary phase calibrator (1.08 degree away from the target). The bright (~ 1 Jy) radio source J2031+1219 was observed as the fringe finder. The estimated VLBI flux densities of the above three calibrators are all obtained from the ASTROGEO Center², where accurate astrometry information can also be found for selecting appropriate calibrators. The main observing cycle is “Cal1 (60s) — Tar (200s) — Cal1 (60s)”. The secondary phase-referencing calibrator was observed for a scan of 200 s every five main cycles, serving as a reference to check the accuracy of the phase-referencing results. In ses-

²<http://www.astrogeo.org>

sions 1 and 3, the observational data at each station were recorded independently in disk modules and shipped to the correlator centre hosted by the Joint Institute for VLBI ERIC (JIVE), located at Dwingeloo, the Netherlands. The total data recording rate is 2 gigabits per second. The disk packs from all stations were shipped to the EVN correlator SFXC⁵⁴. The correlation was carried out using the typical correlation setups for continuum sources (*i.e.*, 1 s integration time and 1 MHz frequency resolution). In the second session (code: RSM04), the data recorded at each station were directly transferred in real time via broad-band optical fibre to the SFXC software correlator in JIVE. Correlation was also carried out in real time mode. The rapid correlation and release of the second-session data enable us to quickly obtain the radio image of AT2019dsg 216 days post burst, validating the successful detection from the VLBI observation.

The correlated data were calibrated by following the standard procedures using the NRAO Astronomical Image Processing System (AIPS) software⁵⁵. After loading the data with task FITLD, the interferometric visibility amplitudes were calibrated using the system temperatures and antenna gain curves measured at each telescope using task ANTAB. For some antennas without system temperature records during the observations, we used the nominal values of the system equivalent flux density in the EVN status table instead. The beginning 30 s of each scan were flagged due to the occupation of antenna slewing. The ionospheric dispersive delays were corrected using a map of total electron content provided by Global Positioning System satellite observations³ and applied to the visibilities through task TECOR. The VLBA procedure task VLBAPANG was used to correct phase variations caused by parallactic angles. A manual phase calibration and bandpass calibra-

³the model files were downloaded from <https://cddis.nasa.gov/archive/gps/products/ionex>

tion were carried out using the best scans of the fringe finder through task FRING and BPASS. The global fringe-fitting was then performed on the phase-referencing calibrator J2052+1619.

After fringe-fitting of the primary phase-referencing calibrator, their visibility data were exported from AIPS and imported into Caltech Difmap software package⁵⁶ for self-calibration and imaging. The corresponding antenna gain corrections from amplitude self-calibration were applied to the data in AIPS. Additional iteration of fringe-fitting was performed on the phase-referencing calibrator by taking account of its CLEAN component model to remove the small phase variations due to the core-jet structure of the phase calibrator. Then the obtained solutions were finally interpolated and applied to the secondary calibrator and the target source using CLCAL. The calibrated data were split into single-source files and imported into Difmap for imaging and model-fitting. The above data reduction and imaging procedures are the same for all sessions. During the data processing, we found that some small antennas have relatively large phase errors due to the coherent loss, we thus excluded these antennas to maintain more accurate measurements on source peak intensities. The antenna participation are shown in table 1. Given the weakness of the target sources, no self-calibration was conducted on it. After CLEANing the peak regions of the map (*i.e.*, signal-to-noise level $\geq 5\sigma$), natural grid weighting was used to create the final images. We used the Modelfit procedure in Difmap to constrain the observing parameters of the source (*e.g.*, positions, sizes, flux densities). Circular Gaussian models were used in the model fitting. Table 2 presents the fitting results. Uncertainties in the parameters are calculated based on that expected from an imaging analysis⁵⁷ and include additional inputs. For the peak intensity and integrated flux density, an extra uncertainty of 5 per cent was coupled with the original errors. The size errors

are derived by using the ratio of the minor FWHM size of the synthesised beam to the component SNR (peak intensities divide by r.m.s noises).

An initial target of opportunity (ToO) 3-hr *e*-EVN observation was conducted on 2019 November 12 (216 days after the TDE). The aim was to verify the compactness of the source, to assess the suitability of the phase calibrator, and the potential for long-term monitoring of the source. Owing to the near real-time reception and correlation of the data, we rapidly processed the *e*-EVN data before the first disk-recording EVN data (session 1, observed on 2019 October 27) were correlated.

A compact source was detected with an integrated flux density of 0.674 ± 0.048 mJy. The peak flux density is ≈ 28 times the *rms* noise, providing reliable detection confidence for the first EVN session and offering the promise of detection for another proposed full-disk observation session scheduled three months later.

The first full-array 8-hr EVN observation was conducted on 2019 October 27 (200 days after TDE). It was proposed as a part of a two-epoch monitoring program of AT2019dsg to monitor the flux density and size evolution of the afterglow and to infer a possible proper motion. A compact source of size ≤ 0.17 mas was constrained with an integrated flux density of 0.61 mJy. The flux density is at a similar level with that in the *e*-EVN epoch. The second 8-hr EVN observation was conducted on 2020 February 28 (session 3; 304 days after TDE), mainly to infer any possible proper motion, if the source remains detectable. A compact source was again detected, though with an expanded size of ≤ 0.48 mas and a reduced integrated flux density of 0.44 mJy.

The astrometric position is derived by averaging the peak positions of the three epochs, which is $\alpha(\text{J2000}) = 20^{\text{h}} 57^{\text{m}} 02.96434^{\text{s}} \pm 0.000010^{\text{s}}$ and $\delta(\text{J2000}) = 14^{\circ} 12' 16.29425'' \pm 0.000197''$. The uncertainties are based on the astrometric error of Cal1 (0.13 mas on RA and 0.17 mas on Dec) and the simulated results on astrometric accuracy of VLBI phase-referenced observations ⁵⁸.

Light curve fitting The compiled 5-GHz light curve (see Figure 2) includes data points covering the rising phase and peak ^{14,31}, our three VLBI points and a final point in the declining phase ¹⁹. The latter is the only data point used from Ref[¹⁹]. This is as they note that their VLA flux densities are systematically lower than the e-MERLIN flux densities ³¹. Since our VLBI estimates are likely to be closer to the e-MERLIN values, we mainly use the reported flux densities reported in Ref[¹⁴] and Ref[³¹]. The final data point however can help better constrain the declining slope of the light curve and may be closer to the actual baseline; we thus use this.

The light curve is fitted using the weighted non-linear least squares method with a model of the form $F_{\nu} = F_{\nu_0} + F_{\nu_1}((t/t_p)^{5\alpha_1} + (t/t_p)^{5\alpha_2})^{-1/5}$, with weights based on the flux density measurement errors, the flux density normalisations $0.0 < F_{\nu_0} \leq 0.5$ mJy, $0.0 < F_{\nu_1} \leq 3.0$ mJy, the rising slope $0.0 \leq \alpha_1 \leq 5.0$ and declining slope $-10.0 \leq \alpha_2 \leq 0.0$, a turnover time t_p days and a smoothness parameter fixed at 5. The availability of flux density measurements during the last three epochs based on our EVN observations plays a crucial role in constraining the optically thin declining phase. The fit yields the parameters $F_{\nu_0} = 0.08 \pm 0.02$ mJy, $F_{\nu_1} = 1.26 \pm 0.03$ mJy, $\alpha_1 = 2.1 \pm 0.1$, $\alpha_2 = -2.4 \pm 0.2$. These yield a peak flux density $F_{\nu_p} = 1.18 \pm 0.03$ mJy and an associated peak time $t_p = 155.6 \pm 3.8$ days.

To refine the results of the light curve fitting described above, we employed a Markov Chain Monte Carlo (MCMC) technique for the parameter estimation with the same fitting function, and using the emcee Python package⁵⁹. Uniform priors were chosen and no assumption was made on their statistical distributions. The fitting was initially performed on a full parameter space and later bounded; this includes a flux density $0.0 < F_{\nu_0} \leq 0.4$ mJy, $0.95 < F_{\nu_1} \leq 1.45$ mJy, the rising slope $1.5 \leq \alpha_2 \leq 2.4$ and declining slope $-13.0 \leq \alpha_1 \leq -4.0$, a turnover time $100 \leq t_p \leq 188$ days and the smoothness parameter fixed at 5. Figure 3 shows the posterior probability on the fit parameters for the MCMC fitting. The fit yields parameters $F_{\nu_0} = 0.05^{+0.06}_{-0.09}$ mJy, $F_{\nu_1} = 1.31^{+0.11}_{-0.10}$ mJy, $\alpha_1 = 2.10^{+0.59}_{-0.50}$ and $\alpha_2 = -1.95^{+0.33}_{-0.36}$. A peak flux density $F_{\nu_p} = 1.19 \pm 0.10$ mJy and an associated peak time $t_p = 159.89^{+7.76}_{-6.91}$ days were obtained.

Afterglow: equipartition estimates and radiative evolution The radio afterglow emission is considered to originate from a non-relativistic spherically expanding forward shock. In this formulation^{32,35}, the peak of the light curve corresponds to the transition of the synchrotron emission from optically thick to thin through self-absorption. The relativistic electrons responsible for the radio emission are assumed to have a power law distribution in energy E , with the number per unit energy $N = N_0 E^{-p}$ where N_0 is a constant evaluated at a given time and $p \geq 2$ is the power law index.

The flux densities in the optically thick ($\propto \nu^{5/2}$) and thin ($\propto \nu^{-(p-1)/2}$) regimes are

$$F_\nu = \frac{\pi R^2}{D_L^2} \frac{c_5}{c_6} B^{-1/2} \left(\frac{\nu}{2c_1} \right)^{5/2} \quad (1)$$

$$F_\nu = \frac{4\pi R^3 f}{3D_L^2} c_5 N_0 B^{(p+1)/2} \left(\frac{\nu}{2c_1} \right)^{-(p-1)/2}, \quad (2)$$

where R is the size of the emitting region, D_L is the luminosity distance, B is the magnetic field strength, f is the emission filling factor. The radiative constants c_1 , c_5 and c_6 as functions of p are given by ⁶⁰

$$c_1 = \frac{3e}{4\pi m_e^3 c^5} \quad (3)$$

$$c_5 = \frac{3^{1/2} e^3}{4\pi m_e c^2 (p+1)} \Gamma\left(\frac{p}{4} + \frac{19}{12}\right) \Gamma\left(\frac{p}{4} - \frac{1}{12}\right) \quad (4)$$

$$c_6 = \frac{3^{1/2} e^3}{8\pi m_e} \left(\frac{3e}{2\pi m_e^3 c^5}\right)^{-2} \Gamma\left(\frac{p}{4} + \frac{1}{6}\right) \Gamma\left(\frac{p}{4} + \frac{11}{6}\right) \quad (5)$$

where the electric charge $e = 4.8 \times 10^{-10}$ e.s.u., electron mass $m_e = 9.11 \times 10^{-28}$ g, speed of light $c = 3 \times 10^{10}$ cm s⁻¹, and Γ represents the Gamma function.

The constant energy density term N_0 in eqn. (2) is obtained from the equipartition condition

$$N_0 = \left(\frac{\epsilon_e}{\epsilon_B}\right) \frac{B^2}{8\pi} (p-2) E_l^{p-2}, \quad (6)$$

where ϵ_e and ϵ_B are the fractions of the total energy density in the particle kinetic energy density and in the magnetic field respectively, and $E_l = 0.51$ MeV = 8.2×10^{-7} erg is the electron rest mass energy and is representative of the energy at which the electrons transition to relativistic.

Equating the flux densities from eqns. (1) and (2), and using eqn. (6), the minimal size R_{eq} and magnetic field strength B_{eq} are expressed in terms of the peak flux density F_{ν_p} and correspond-

ing frequency ν_p as

$$R_{eq} = \left(\frac{6c_6^{p+5} F_{\nu_p}^{p+6} D_L^{2p+12}}{(\epsilon_e/\epsilon_B) f(p-2) \pi^{p+5} c_5^{p+6} E_l^{p-2}} \right)^{1/(2p+13)} \left(\frac{\nu_p}{2c_1} \right)^{-1} \quad (7)$$

$$= (1.25 \times 10^{17} \text{ cm}) \left(\frac{F_{\nu_p}}{\text{mJy}} \right)^{8/17} \left(\frac{D_L}{100 \text{ Mpc}} \right)^{16/17} \left(\frac{\epsilon_e}{\epsilon_B} \right)^{-1/17} f^{-1/17} \left(\frac{\nu_p}{\text{GHz}} \right)^{-1}$$

$$B_{eq} = \left(\frac{36\pi^3 c_5}{(\epsilon_e/\epsilon_B)^2 f^2 (p-2)^2 c_5^3 E_l^{2(p-2)} F_{\nu_p} D_L^2} \right)^{2/(2p+13)} \left(\frac{\nu_p}{2c_1} \right) \quad (8)$$

$$= (0.10 \text{ G}) \left(\frac{F_{\nu_p}}{\text{mJy}} \right)^{-2/17} \left(\frac{D_L}{100 \text{ Mpc}} \right)^{-4/17} \left(\frac{\epsilon_e}{\epsilon_B} \right)^{-4/17} f^{-4/17} \left(\frac{\nu_p}{\text{GHz}} \right),$$

and the minimal energy and number density are evaluated as

$$E_{eq} = \frac{B_{eq}^2}{8\pi\epsilon_B} \frac{4\pi}{3} R_{eq}^3 f \quad (9)$$

$$= (3.46 \times 10^{48} \text{ erg}) \left(\frac{F_{\nu_p}}{\text{mJy}} \right)^{20/17} \left(\frac{D_L}{100 \text{ Mpc}} \right)^{40/17} \left(\frac{\epsilon_e}{\epsilon_B} \right)^{-11/17} \epsilon_B^{-1} f^{6/17} \left(\frac{\nu_p}{\text{GHz}} \right)^{-1}$$

$$n_{eq} = \frac{\epsilon_e}{\epsilon_B} \frac{B_{eq}^2}{8\pi} \left(\frac{p-2}{p-1} \right) E_l^{-1} \quad (10)$$

$$= (5.11 \text{ cm}^{-3}) \left(\frac{F_{\nu_p}}{\text{mJy}} \right)^{-4/17} \left(\frac{D_L}{100 \text{ Mpc}} \right)^{-8/17} \left(\frac{\epsilon_e}{\epsilon_B} \right)^{9/17} f^{-8/17} \left(\frac{\nu_p}{\text{GHz}} \right)^2,$$

where the expressions for R_{eq} , B_{eq} , E_{eq} and n_{eq} are evaluated for $p = 2.01$ and assuming fiducial values for the free parameters.

The analysis assumes that the peak frequency ν_p is equal to the synchrotron self-absorption frequency ν_a which is obtained from the condition that the optical depth to self-absorption $\tau \approx \alpha_\nu R = 1$ at $\nu = \nu_a$, where α_ν is the absorption coefficient and R is the time evolving size of the emission region. The time dependent physical parameters include $R \propto t^\alpha = R_{eq}(t/t_p)^\alpha$, $B \propto R^{-2} \propto t^{-2\alpha} = B_{eq}(t/t_p)^{-2\alpha}$ and $N_0 \propto B^2 = N_{0,eq}(t/t_p)^{-4\alpha}$ where $N_{0,eq} = N_0(B = B_{eq})$ (see eqn. 6); t_p is the time associated with the light curve peak.

The absorption coefficient is

$$\alpha_\nu = c_6 N_0 B^{(p+2)/2} \left(\frac{\nu}{2c_1} \right)^{-(p+4)/2}. \quad (11)$$

Using the condition $\alpha_\nu R = 1$ and the time dependent parameters, the synchrotron self-absorption frequency is

$$\nu_a = 2c_1 (R c_6 N_0)^{2/(p+4)} B^{(p+2)/(p+4)} \propto t^{-2(p+5)/(p+4)} \quad (12)$$

$$= (0.97 \times 10^9 \text{ Hz}) \left(\frac{\epsilon_e}{\epsilon_B} \right)^{-17/51} f^{-16/51} \left(\frac{\nu_p}{\text{GHz}} \right) \left(\frac{t}{t_p} \right)^{-7\alpha/3} \quad (13)$$

The characteristic synchrotron frequency emitted by a relativistic electron with a Lorentz factor γ_e is

$$\nu_e = \frac{eB\gamma_e^2}{2\pi m_e c}. \quad (14)$$

For $\gamma_e = \gamma_m = \left(\frac{p-2}{p-1} \right) \left(\frac{m_p}{m_e} \right) \epsilon_e$, the minimum injected Lorentz factor, the corresponding synchrotron frequency is

$$\begin{aligned} \nu_m &= \frac{eB\gamma_m^2}{2\pi m_e c} \propto t^{-2\alpha} \\ &= (9.03 \times 10^7 \text{ Hz}) \left(\frac{F_{\nu_p}}{\text{mJy}} \right)^{-2/17} \left(\frac{D_L}{100 \text{ Mpc}} \right)^{-4/17} \left(\frac{\epsilon_e}{\epsilon_B} \right)^{-4/17} \epsilon_e^2 f^{-4/17} \left(\frac{\nu_p}{\text{GHz}} \right) \left(\frac{t}{t_p} \right)^{-2\alpha}, \end{aligned} \quad (15)$$

while for $\gamma_e = \gamma_c = \frac{6\pi m_e c}{\sigma_T B^2 t}$, the critical Lorentz factor above which synchrotron cooling dominates and where $\sigma_T = 6.65 \times 10^{-25} \text{ cm}^2$ is the Thomson cross section, the corresponding synchrotron cooling frequency is

$$\begin{aligned} \nu_c &= \frac{18\pi m_e c e}{\sigma_T^2 (1+z) B^3 t^2} \propto t^{6\alpha-2} \\ &= (1.97 \times 10^{17} \text{ Hz}) \left(\frac{F_{\nu_p}}{\text{mJy}} \right)^{6/17} \left(\frac{D_L}{100 \text{ Mpc}} \right)^{-12/17} \left(\frac{\epsilon_e}{\epsilon_B} \right)^{12/17} f^{12/17} \left(\frac{\nu_p}{\text{GHz}} \right)^{-3} \left(\frac{t}{t_p} \right)^{6\alpha} \left(\frac{t}{\text{day}} \right)^{-2}. \end{aligned} \quad (16)$$

Accretion Post the TDE, most gravitationally bound stellar material returns to the pericentre when orbiting the SMBH. The fallback timescale is⁵

$$t_{\text{fb}} = (41 \text{ days}) M_6^{1/2} m_\star^{(1-3\xi)/2} \beta^{-3}, \quad (17)$$

assuming that the main-sequence mass-radius relationship $R_\star = R_\odot m_\star^{1-\xi}$ ⁶¹ is valid for the disrupted star with a scaled mass $m_\star = M_\star/M_\odot$ and radius R_\star , where the index $\xi \approx 0.4$ for $m_\star \geq 1.0$ ⁽⁶²⁾. The other scaled quantities include $M_6 = M_\bullet/(10^6 M_\odot)$ and a penetration factor $\beta \equiv R_t/R_p$ defined as the ratio of the tidal radius of the SMBH R_t to the pericentre distance R_p .

The tidal radius of the SMBH R_t can be expressed in terms of the SMBH mass and stellar properties² as

$$R_t \approx \left(\frac{M_\bullet}{M_\star} \right)^{1/3} R_\star = (6.95 \times 10^{12} \text{ cm}) M_6^{1/3} m_\star^{(2/3)-\xi}, \quad (18)$$

which is then scaled in terms of the Schwarzschild radius $R_S = 2GM_\bullet/c^2 = (2.95 \times 10^{11} \text{ cm}) M_6$, as

$$(R_t/R_S) = (23.58) M_6^{-2/3} m_\star^{(2/3)-\xi}. \quad (19)$$

The distance of the closest approach to the SMBH is the pericentre distance $R_p \geq 3R_S$, the innermost stable circular orbit for a non-rotating Schwarzschild black hole. With $R_t \geq R_p$, $R_t/R_S \geq R_p/R_S \geq 3$, the penetration factor $\beta \equiv R_t/R_p$ is in the range $1 \leq \beta \leq (7.86) M_6^{-2/3} m_\star^{(2/3)-\xi}$.

The fallback accretion rate onto the SMBH² is

$$\dot{M}_{\text{fb}} = \frac{1}{3} \frac{M_\star}{t_{\text{fb}}} \left(\frac{t}{t_{\text{fb}}} \right)^{-5/3}, \quad (20)$$

at a time t post the tidal disruption. The peak rate corresponds to $t = t_{\text{fb}}$ where

$$\dot{M}_{\text{p}} = \dot{M}_{\text{fb}}|_{t=t_{\text{fb}}} \approx (3.0 M_\odot \text{ yr}^{-1}) M_6^{-1/2} m_\star^{(1+3\xi)/2} \beta^3. \quad (21)$$

The Eddington accretion rate is

$$\dot{M}_{\text{Edd}} = \frac{L_{\text{Edd}}}{\epsilon c^2} = \frac{4\pi G M_{\bullet} m_p}{\epsilon c \sigma_T} = (0.023 M_{\odot} \text{yr}^{-1}) M_6, \quad (22)$$

for an assumed efficiency factor which we fix at a fiducial value $\epsilon = 0.1$ and where $\sigma_T = 6.65 \times 10^{-25} \text{ cm}^2$ is the Thomson cross section for electron scattering. Using the scaling $t_d = t/(1 \text{ day})$, the fallback accretion rate and peak rate are super Eddington (see Eq. 20 and Eq. 21), with

$$\dot{m}_{\text{fb}} = (\dot{M}_{\text{fb}}/\dot{M}_{\text{Edd}}) = (6.34 \times 10^4) M_6^{-2/3} m_{\star}^{(4-3\xi)/3} \beta^{-2} t_d^{-5/3} \quad (23)$$

$$\dot{m}_{\text{p}} = (\dot{M}_{\text{p}}/\dot{M}_{\text{Edd}}) = (130.43) M_6^{-3/2} m_{\star}^{(1+3\xi)/2} \beta^3. \quad (24)$$

Outflow and photospheric properties During the super-Eddington accretion phase, the returning tidal stream post the stellar disruption can encounter the stellar debris being accreted onto the SMBH, resulting in a shocked debris and the subsequent launching of outflows^{44,63,64}. The outflow is expected to be launched close to the circularization radius of the accreted material $R_C \approx 2R_p = 2R_t \beta^{-1}$ with an initial velocity⁶,

$$v_w \approx \left(\frac{GM_{\bullet}}{R_C} \right)^{1/2} = (0.1 c) M_6^{1/3} m_{\star}^{-(1/3-\xi/2)} \beta^{1/2}, \quad (25)$$

with the equality corresponding to the escape velocity at the radius R_C . Assuming that the efficiency for mass-energy conversion during circularization is 1 %, the associated timescale is⁴³

$$t_{\text{circ}} = (1.8 \times 10^6 \text{ s}) \beta^{-3/2} M_6^{-1/2} m^{3(1-2\xi)/2}. \quad (26)$$

The fallback accretion rate declines as $t^{-5/3}$ (see Eq. 23) with $\dot{M}_{\text{fb}} = \dot{M}_{\text{Edd}}$ denoting a transition from the super-Eddington to the sub-Eddington regime. The corresponding timescale t_j

is taken to be the lifetime of the outflow and is given by,

$$t_j = (6.54 \times 10^7 \text{ s}) M_6^{-2/5} m_\star^{(4-3\xi)/5} \beta^{-6/5}. \quad (27)$$

With the above outflow velocity v_w and $n \propto (R/R_{eq})^{-\gamma} = n_{eq}(t/t_p)^{-\gamma\alpha}$ to represent the number density decline with distance $R = R_{eq}(t/t_p)^\alpha$, the mass outflow rate is

$$\dot{M}_w = 4\pi R^2 v_w n m_p \quad (28)$$

$$= (8.0 \times 10^{-5} M_\odot \text{ yr}^{-1}) M_6^{1/3} m_\star^{-(1/3-\xi/2)} \beta^{1/2} \left(\frac{F_{\nu_p}}{\text{mJy}} \right)^{12/17} \left(\frac{D_L}{100 \text{ Mpc}} \right)^{24/17} \left(\frac{\epsilon_e}{\epsilon_B} \right)^{7/17} f^{-10/17} \left(\frac{t}{t_p} \right)^{\alpha(2-\gamma)}. \quad (29)$$

An upper limit on the particle number density in the vicinity of the accretion disk is based on the unbound stellar debris that is spatially and kinematically distributed in this region ⁶

$$n_a \leq (1.46 \times 10^{18} \text{ cm}^{-3}) M_6^{1/6} m_\star^{(5/6)-(3\xi/2)} t_d^{-3}. \quad (30)$$

Assuming that the constituent gas in the outflow is in thermal equilibrium with a consequent black-body spectrum, the total luminosity is approximated by the Stefan-Boltzmann law⁶ such that

$$L_j = \sigma_{\text{SB}} (4\pi R_{\text{ph}}^2) T_{\text{ph}}^4 = (6.68 \times 10^{44} \text{ erg s}^{-1}) M_6^{8/9} m_\star^{(2-\xi)/6} \beta^{-2/3} t_d^{-5/9}, \quad (31)$$

where $\sigma_{\text{SB}} = 5.67 \times 10^{-5} \text{ erg cm}^{-2} \text{ s}^{-1} \text{ K}^{-4}$ is the Stefan-Boltzmann constant, a photospheric radius R_{ph} and an associated thermal temperature T_{ph} ,

$$R_{\text{ph}} = (6.3 \times 10^{16} \text{ cm}) m_\star^{5/3-3\xi/2} \beta^{-2} t_d^{-5/3} \quad (32)$$

$$T_{\text{ph}} = (1.25 \times 10^3 \text{ K}) M_6^{2/9} m_\star^{3/4-17\xi/24} \beta^{5/6} t_d^{25/36}, \quad (33)$$

assuming a mass outflow rate $\dot{M}_w \leq 0.1 \dot{M}_{\text{fb}}$ ^{65,66} and the equality in Eq. 25. Also employed in the above equation are the expressions for $R_p/(3R_S)$ and \dot{m}_{fb} from Eq. 18 and Eq. 23, respectively. The corresponding total kinetic energy E_j is estimated using the above thermal luminosity and an additive component from the power-law tail during the declining phase,

$$E_j = \int_0^{t_j} L_j dt + \int_{t_j}^t L_j (t/t_j)^{-5/3} dt \approx (3.81 \times 10^{51} \text{ erg}) M_6^{32/45} m_\star^{(62-39\xi)/90} \beta^{-6/5}. \quad (34)$$

The number density of material in the outflow is given by

$$n_j = \frac{L_j}{4\pi R^2 m_p c^3}. \quad (35)$$

Using L_j from Eq. 31 and the scalings $n = n_{eq}(t/t_p)^{-\gamma\alpha}$ and $R = R_{eq}(t/t_p)$, the density contrast between the CNM and the outflow,

$$\kappa = \frac{n}{n_j} = (6.78 \times 10^{-2}) M_6^{-8/9} m_\star^{-(2-\xi)/6} \beta^{2/3} \left(\frac{F_{\nu_p}}{\text{mJy}} \right)^{12/17} \left(\frac{D_L}{100 \text{ Mpc}} \right)^{24/17} \left(\frac{\epsilon_e}{\epsilon_B} \right)^{7/17} f^{-10/17} t_{\text{day}}^{5/9}, \quad (36)$$

where a $\gamma = 2$ is adopted.

The maximum energy to which protons can be accelerated by the outflow is limited by comparing the associated timescale with the dynamical timescale⁴⁵. Using the scalings for the size, velocity and magnetic field strength in the emission region, the maximum energy is

$$\begin{aligned} E_p &\leq \frac{3v^2}{20c^2} eBct = \frac{3}{20} \frac{e\alpha^2}{ct} R_{eq}^2 B_{eq} \\ &\leq (6.63 \times 10^{18} \text{ eV}) \left(\frac{F_{\nu_p}}{\text{mJy}} \right)^{14/17} \left(\frac{D_L}{100 \text{ Mpc}} \right)^{28/17} \left(\frac{\epsilon_e}{\epsilon_B} \right)^{-6/17} f^{-6/17} \left(\frac{\nu_p}{\text{GHz}} \right)^{-1} \left(\frac{t}{\text{day}} \right)^{-1} \end{aligned} \quad (37)$$

The maximum energy to which protons can be accelerated during the radiatively inefficient accretion flow is limited by comparing the timescale for plasma turbulence acceleration with the

diffusion timescale⁴³. Using the photospheric radius $R = R_{ph}$, and assuming a plasma beta of 3, and a proton number density equal to the particle number density calculated above, the maximum energy of protons is⁴³,

$$E_p \leq \frac{2\pi^{1/2}e}{3} \left(\frac{R}{R_S} \right)^{-1} R_S (m_p n_p c^2)^{1/2} \quad (38)$$

$$E_p \leq (2.33 \times 10^{16} \text{ eV}) M_6^{25/12} m_\star^{-(5/4)-(9\xi/8)} \beta^2 \left(\frac{t}{\text{day}} \right)^{1/6}.$$

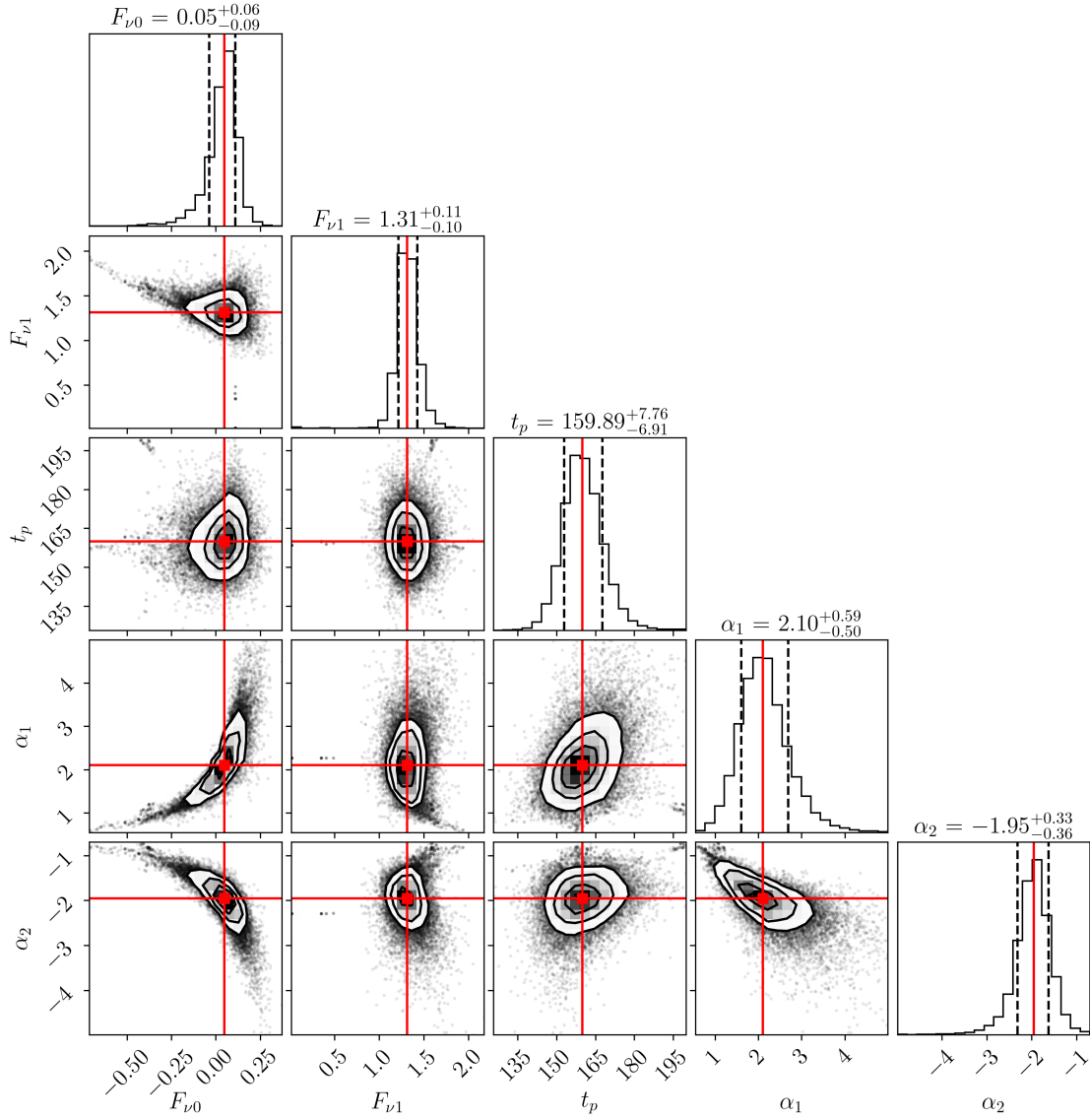


Figure 3: Results from the MCMC fitting of the 5 GHz light curve. The corner plot shows the posterior probability distribution of parameters from the fitting. The best-fit values (maximum posterior probability) are shown in red colour. Dotted lines mark 16, 50 and 84 per cent of the marginalized posteriors for each parameter. The values are labeled in the title of each sub-panel.

Table 1: EVN 5-GHz observations of AT2019dsg.

Code	Date	Array	τ_{int} (min)	θ_{beam} (mas, mas, °)	σ (mJy beam ⁻¹)	Telescopes
EM140A	2019 10 27	full EVN ¹	255	6.1×0.9 at 9.6°	0.015	Out: Ir Flag: Sv,Zc,Hh,Wb
RSM04	2019 11 12	e-EVN ²	105	8.6×2.3 at -13.2°	0.024	Out: Sv, Ur, Km Flag: Zc,Hh,Wb,Cm,De
EM140B	2020 02 28	full EVN	255	5.3×1.3 at 6.5°	0.016	Out: Ur, Km Flag: Sv,Zc,Hh,Wb

Note: Column 1–Project code; Column 2–Observation date; Column 3–VLBI network; Column 4–Integration time of the target; Column 5–Synthesised beam size (major, minor and position angle of the major axis); Column 6–Post-clean *rms* noise in the image; Column 7–Notifications for participating antennas.

¹EVN telescopes participating the observation are: Bd (Badary 32m, Russia), Ef (Effelsberg 100m, Germany), Hh (Hartebeesthoek 26m, South Africa), Ir (Irbene 16m, Latvia), Jb (Lovell 76m, UK), Km (Kunming 40m, China), Mc (Medicina 25m, Italy), On85 (Onsala 25m, Sweden), Sv (Svetloe 32m, Russia), T6 (Tianma 65m, China), Tr (Torun 32m, Poland), Ur (Urumqi 26m, China), Wb (Westerbork 25m, Netherlands), Ys (Yebes 40m, Spain), Zc (Zelenchukskaya 32m, Russia).

²For e-EVN, 5 extra antennas from e-MERLIN are included in the above array: Cm (Cambridge 32m, UK), Da (Darnhall 25m, UK), De (Defford 25m, UK), Kn (Knockin 25m, UK), Pi (Pickmere 25m, UK).

Table 2: Imaging parameters of AT2019dsg

Session	MJD	t_{post}	S_{peak}	S_{int}	θ_{FWHM}	T_{B}
	(day)	(day)	(mJy beam $^{-1}$)	(mJy)	(mas)	(K)
EM140a	58783.6	200	0.598 ± 0.034	0.608 ± 0.037	0.17 ± 0.02	1.1×10^9
RSM04	58799.6	216	0.651 ± 0.040	0.674 ± 0.048	≤ 0.60	$\geq 9.8 \times 10^7$
EM140b	58907.3	304	0.442 ± 0.027	0.442 ± 0.032	≤ 0.48	$\geq 1.0 \times 10^8$

Note: Column 1–Session code; Column 2–Observation time in Modified Julian Dates (MJD); Column 3–Day after the TDE burst; Column 4–Peak intensity of the detected source; Column 5–Integrated flux density of the fitted Gaussian component; Column 6–The full width at half maximum (FWHM) size of the fitted circular Gaussian component; Column 7–Brightness temperature of the fitted component.

1. Rees, M. J. Tidal disruption of stars by black holes of 10^6 - 10^8 solar masses in nearby galaxies. *Nature* **333**, 523–528 (1988).
2. Evans, C. R. & Kochanek, C. S. The Tidal Disruption of a Star by a Massive Black Hole. *Astrophys. J. Lett.* **346**, L13 (1989).
3. Saxton, R., Komossa, S., Auchettl, K. & Jonker, P. G. X-Ray Properties of TDEs. *Space Sci. Rev.* **216**, 85 (2020).
4. Phinney, E. S. Manifestations of a Massive Black Hole in the Galactic Center. In Morris, M. (ed.) *The Center of the Galaxy*, vol. 136, 543 (1989).
5. Lodato, G. & Rossi, E. M. Multiband light curves of tidal disruption events. *Mon. Not. R. Astron. Soc.* **410**, 359–367 (2011).
6. Strubbe, L. E. & Quataert, E. Optical flares from the tidal disruption of stars by massive black holes. *Mon. Not. R. Astron. Soc.* **400**, 2070–2084 (2009).
7. Mattila, S. *et al.* A dust-enshrouded tidal disruption event with a resolved radio jet in a galaxy merger. *Science* **361**, 482–485 (2018).
8. Roth, N. *et al.* Radiative Emission Mechanisms. *Space Sci. Rev.* **216**, 114 (2020). [2008.01117](#).
9. Yang, J. *et al.* No apparent superluminal motion in the first-known jetted tidal disruption event Swift J1644+5734. *Mon. Not. R. Astron. Soc.* **462**, L66–L70 (2016).

10. Alexander, K. D., van Velzen, S., Horesh, A. & Zauderer, B. A. Radio Properties of Tidal Disruption Events. *Space Sci. Rev.* **216**, 81 (2020).
11. Nordin, J. *et al.* ZTF Transient Discovery Report for 2019-04-22. *Transient Name Server Discovery Report* **2019-615**, 1 (2019).
12. Nicholl, M. *et al.* ePESSTO+ classification of optical transients. *The Astronomer's Telegram* **12752**, 1 (2019).
13. van Velzen, S. *et al.* Seventeen Tidal Disruption Events from the First Half of ZTF Survey Observations: Entering a New Era of Population Studies. *Astrophys. J.* **908**, 4 (2021). [2001.01409](#).
14. Stein, R. *et al.* A tidal disruption event coincident with a high-energy neutrino. *Nat. Astron* (2021).
15. IceCube Collaboration. IceCube-191001A - IceCube observation of a high-energy neutrino candidate event. *GRB Coordinates Network* **25913**, 1 (2019).
16. Lee, C.-H. *et al.* Optical Polarimetry of the Tidal Disruption Event AT2019DSG. *Astrophys. J. Lett.* **892**, L1 (2020).
17. Winter, W. & Lunardini, C. A concordance scenario for the observed neutrino from a tidal disruption event. *Nature Astronomy* **5**, 472–477 (2021). [2005.06097](#).
18. Liu, R.-Y., Xi, S.-Q. & Wang, X.-Y. Neutrino emission from an off-axis jet driven by the tidal disruption event AT2019dsg. *Phys. Rev. D* **102**, 083028 (2020).

19. Cendes, Y. *et al.* Radio Observations of an Ordinary Outflow from the Tidal Disruption Event AT2019dsg. *arXiv e-prints* arXiv:2103.06299 (2021). [2103.06299](#).
20. Mohan, P., An, T. & Yang, J. The Nearby Luminous Transient AT2018cow: A Magnetar Formed in a Subrelativistically Expanding Nonjetted Explosion. *Astrophys. J. Lett.* **888**, L24 (2020).
21. Levan, A. J. *et al.* An Extremely Luminous Panchromatic Outburst from the Nucleus of a Distant Galaxy. *Science* **333**, 199 (2011).
22. Zauderer, B. A. *et al.* Birth of a relativistic outflow in the unusual γ -ray transient Swift J164449.3+573451. *Nature* **476**, 425–428 (2011).
23. Berger, E. *et al.* Radio Monitoring of the Tidal Disruption Event Swift J164449.3+573451. I. Jet Energetics and the Pristine Parsec-scale Environment of a Supermassive Black Hole. *Astrophys. J.* **748**, 36 (2012). [1112.1697](#).
24. Zauderer, B. A. *et al.* Radio Monitoring of the Tidal Disruption Event Swift J164449.3+573451. II. The Relativistic Jet Shuts Off and a Transition to Forward Shock X-Ray/Radio Emission. *Astrophys. J.* **767**, 152 (2013). [1212.1173](#).
25. Eftekhari, T., Berger, E., Zauderer, B. A., Margutti, R. & Alexander, K. D. Radio Monitoring of the Tidal Disruption Event Swift J164449.3+573451. III. Late-time Jet Energetics and a Deviation from Equipartition. *Astrophys. J.* **854**, 86 (2018). [1710.07289](#).

26. Cendes, Y., Eftekhari, T., Berger, E. & Polisensky, E. Radio Monitoring of the Tidal Disruption Event Swift J164449.3+573451. IV. Continued Fading and Non-relativistic Expansion. *Astrophys. J.* **908**, 125 (2021). [2011.00074](#).
27. van Velzen, S. *et al.* A radio jet from the optical and x-ray bright stellar tidal disruption flare ASASSN-14li. *Science* **351**, 62–65 (2016). [1511.08803](#).
28. Alexander, K. D., Berger, E., Guillochon, J., Zauderer, B. A. & Williams, P. K. G. Discovery of an Outflow from Radio Observations of the Tidal Disruption Event ASASSN-14li. *Astrophys. J. Lett.* **819**, L25 (2016).
29. Romero-Cañizales, C. *et al.* The TDE ASASSN-14li and Its Host Resolved at Parsec Scales with the EVN. *Astrophys. J. Lett.* **832**, L10 (2016).
30. Bright, J. S. *et al.* Long-term radio and X-ray evolution of the tidal disruption event ASASSN-14li. *Mon. Not. R. Astron. Soc.* **475**, 4011–4019 (2018). [1801.03094](#).
31. Cannizzaro, G. *et al.* Accretion disc cooling and narrow absorption lines in the tidal disruption event AT 2019dsg. *Mon. Not. R. Astron. Soc.* **504**, 792–815 (2021). [2012.10195](#).
32. Anderson, M. M. *et al.* Caltech-NRAO Stripe 82 Survey (CNSS). III. The First Radio-discovered Tidal Disruption Event, CNSS J0019+00. *Astrophys. J.* **903**, 116 (2020).
33. Wright, E. L. A Cosmology Calculator for the World Wide Web. *PASP* **118**, 1711–1715 (2006).

34. Scott, M. A. & Readhead, A. C. S. The low-frequency structure of powerful radio sources and limits to departures from equipartition. *Mon. Not. R. Astron. Soc.* **180**, 539–550 (1977).
35. Chevalier, R. A. Synchrotron Self-Absorption in Radio Supernovae. *Astrophys. J.* **499**, 810–819 (1998).
36. Ho, A. Y. Q. *et al.* AT2018cow: A Luminous Millimeter Transient. *Astrophys. J.* **871**, 73 (2019). [1810.10880](#).
37. Mohan, P. & Mangalam, A. Kinematics of and Emission from Helically Orbiting Blobs in a Relativistic Magnetized Jet. *Astrophys. J.* **805**, 91 (2015). [1503.06551](#).
38. Yang, J. *et al.* The nearby extreme accretion and feedback system PDS 456: finding a complex radio-emitting nucleus. *Mon. Not. R. Astron. Soc.* **500**, 2620–2626 (2021). [2008.05194](#).
39. Krolik, J., Piran, T., Svirski, G. & Cheng, R. M. ASASSN-14li: A Model Tidal Disruption Event. *Astrophys. J.* **827**, 127 (2016). [1602.02824](#).
40. Farrar, G. R. & Gruzinov, A. Giant AGN Flares and Cosmic Ray Bursts. *Astrophys. J.* **693**, 329–332 (2009). [0802.1074](#).
41. Guépin, C., Kotera, K., Barausse, E., Fang, K. & Murase, K. Ultra-high-energy cosmic rays and neutrinos from tidal disruptions by massive black holes. *Astron. Astrophys.* **616**, A179 (2018). [1711.11274](#).

42. Biehl, D., Boncioli, D., Lunardini, C. & Winter, W. Tidally disrupted stars as a possible origin of both cosmic rays and neutrinos at the highest energies. *Scientific Reports* **8**, 10828 (2018). [1711.03555](#).
43. Hayasaki, K. & Yamazaki, R. Neutrino Emissions from Tidal Disruption Remnants. *Astrophys. J.* **886**, 114 (2019). [1908.10882](#).
44. Murase, K., Kimura, S. S., Zhang, B. T., Oikonomou, F. & Petropoulou, M. High-energy Neutrino and Gamma-Ray Emission from Tidal Disruption Events. *Astrophys. J.* **902**, 108 (2020).
45. Zhang, B. T., Murase, K., Oikonomou, F. & Li, Z. High-energy cosmic ray nuclei from tidal disruption events: Origin, survival, and implications. *Phys. Rev. D* **96**, 063007 (2017). [1706.00391](#).
46. Mannheim, K. The proton blazar. *Astron. Astrophys.* **269**, 67–76 (1993).
47. Giommi, P. *et al.* Dissecting the regions around IceCube high-energy neutrinos: growing evidence for the blazar connection. *Mon. Not. R. Astron. Soc.* **497**, 865–878 (2020).
48. Murase, K. & Waxman, E. Constraining high-energy cosmic neutrino sources: Implications and prospects. *Phys. Rev. D* **94**, 103006 (2016). [1607.01601](#).
49. Hooper, D., Linden, T. & Vieregg, A. Active galactic nuclei and the origin of IceCube’s diffuse neutrino flux. *J. Cosmology Astropart. Phys.* **2019**, 012 (2019). [1810.02823](#).

50. Rachen, J. P. & Mészáros, P. Photohadronic neutrinos from transients in astrophysical sources. *Phys. Rev. D* **58**, 123005 (1998). [astro-ph/9802280](#).
51. Waxman, E. & Bahcall, J. High energy neutrinos from astrophysical sources: An upper bound. *Phys. Rev. D* **59**, 023002 (1999). [hep-ph/9807282](#).
52. Guépin, C. & Kotera, K. Can we observe neutrino flares in coincidence with explosive transients? *Astron. Astrophys.* **603**, A76 (2017).
53. Beasley, A. J. & Conway, J. E. VLBI Phase-Referencing. In Zensus, J. A., Diamond, P. J. & Napier, P. J. (eds.) *Very Long Baseline Interferometry and the VLBA*, vol. 82 of *Astronomical Society of the Pacific Conference Series*, 327 (1995).
54. Keimpema, A. *et al.* The SFXC software correlator for very long baseline interferometry: algorithms and implementation. *Experimental Astronomy* **39**, 259–279 (2015).
55. Greisen, E. W. *AIPS, the VLA, and the VLBA*, vol. 285, 109 (2003).
56. Shepherd, M. C. Difmap: an Interactive Program for Synthesis Imaging. In Hunt, G. & Payne, H. (eds.) *Astronomical Data Analysis Software and Systems VI*, vol. 125 of *Astronomical Society of the Pacific Conference Series*, 77 (1997).
57. Fomalont, E. B. Image Analysis. In Taylor, G. B., Carilli, C. L. & Perley, R. A. (eds.) *Synthesis Imaging in Radio Astronomy II*, vol. 180 of *Astronomical Society of the Pacific Conference Series*, 301 (1999).

58. Pradel, N., Charlot, P. & Lestrade, J. F. Astrometric accuracy of phase-referenced observations with the VLBA and EVN. *Astron. Astrophys.* **452**, 1099–1106 (2006). [astro-ph/0603015](#).
59. Foreman-Mackey, D., Hogg, D. W., Lang, D. & Goodman, J. emcee: The MCMC Hammer. *PASP* **125**, 306 (2013). [1202.3665](#).
60. Pacholczyk, A. G. *Radio astrophysics. Nonthermal processes in galactic and extragalactic sources* (1970).
61. Kippenhahn, R. & Weigert, A. *Stellar Structure and Evolution* (1994).
62. Krolik, J. H. & Piran, T. Jets from Tidal Disruptions of Stars by Black Holes. *Astrophys. J.* **749**, 92 (2012).
63. Jiang, Y.-F., Guillochon, J. & Loeb, A. Prompt Radiation and Mass Outflows from the Stream-Stream Collisions of Tidal Disruption Events. *Astrophys. J.* **830**, 125 (2016).
64. Lu, W. & Bonnerot, C. Self-intersection of the fallback stream in tidal disruption events. *Mon. Not. R. Astron. Soc.* **492**, 686–707 (2020).
65. Mageshwaran, T. & Mangalam, A. Stellar and Gas Dynamical Model for Tidal Disruption Events in a Quiescent Galaxy. *Astrophys. J.* **814**, 141 (2015).
66. Mageshwaran, T. & Mangalam, A. Dynamics of accretion and winds in tidal disruption events. *New A* **83**, 101491 (2021).

Acknowledgements This work is supported by National Key R&D Programme of China (grant number 2018YFA0404603). The European VLBI Network (EVN) is a joint facility of independent European, African, Asian, and North American radio astronomy institutes. Scientific results from data presented in this publication are derived from the following EVN project code(s): EM140, RSM04. We thank Wen Chen at Kunming Station for making the first observation. e-VLBI research infrastructure in Europe is supported by the European Union, Seventh Framework Programme (FP7/2007-2013) under grant agreement number RI-261525 NEXPreS. e-MERLIN is a National Facility operated by the University of Manchester at Jodrell Bank Observatory on behalf of STFC. The VLBI data processing made use of the compute resource of the China SKA Regional Centre prototype, funded by the Ministry of Science and Technology of China and the Chinese Academy of Sciences.

Author Contribution P.M. and T.A. designed the VLBI observations, interpreted the results, and drafted the manuscript. With help from J.Y, Y.-K.Z. conducted the VLBI observation and worked on the data reduction. Y.-K.Z. contributed to writing the Methods section. X.-L.Y. contributed to the MCMC fitting. A.-L.W. contributed to preparing the figures. All the authors discussed the results and commented on the manuscript.

Competing Interests The authors declare that they have no competing financial interests.

Correspondence Correspondence and requests for materials should be addressed to P. M. (email: pmohan@shao.ac.cn) or T. A. (email: antao@shao.ac.cn).